

## Durham Research Online

---

### Deposited in DRO:

18 September 2020

### Version of attached file:

Published Version

### Peer-review status of attached file:

Peer-reviewed

### Citation for published item:

Xu, Wenxiao and Guo, Qi and Zheng, Haonan and Gao, Liang and Lacey, Cedric and Gu, Qing and Liao, Shihong and Shao, Shi and Mao, Tianxiang and Zhang, Tianchi and Chen, Xuelei (2020) 'Galaxy properties in the cosmic web of EAGLE simulation.', *Monthly notices of the Royal Astronomical Society.*, 498 (2). pp. 1839-1851.

### Further information on publisher's website:

<https://doi.org/10.1093/mnras/staa2497>

### Publisher's copyright statement:

This article has been accepted for publication in *Monthly notices of the Royal Astronomical Society*. ©: 2020 The Author(s). Published by Oxford University Press on behalf of the Royal Astronomical Society. All rights reserved.

### Additional information:

---

### Use policy

The full-text may be used and/or reproduced, and given to third parties in any format or medium, without prior permission or charge, for personal research or study, educational, or not-for-profit purposes provided that:

- a full bibliographic reference is made to the original source
- a [link](#) is made to the metadata record in DRO
- the full-text is not changed in any way

The full-text must not be sold in any format or medium without the formal permission of the copyright holders.

Please consult the [full DRO policy](#) for further details.

# Galaxy properties in the cosmic web of EAGLE simulation

Wenxiao Xu,<sup>1,2</sup> Qi Guo,<sup>1,2</sup>★ Haonan Zheng,<sup>1,2</sup> Liang Gao,<sup>1,2</sup> Cedric Lacey<sup>3</sup>, Qing Gu,<sup>1,2</sup> Shihong Liao<sup>1</sup>, Shi Shao<sup>3</sup>, Tianxiang Mao<sup>1,2</sup>, Tianchi Zhang<sup>1,2</sup> and Xuelei Chen<sup>1,2</sup>

<sup>1</sup>Key Laboratory for Computational Astrophysics, National Astronomical Observatories, Chinese Academy of Sciences, Beijing 100012, China

<sup>2</sup>School of Astronomy and Space Science, University of Chinese Academy of Sciences, Beijing 100049, China

<sup>3</sup>Institute for Computational Cosmology, Department of Physics, Durham University, South Road, Durham DH1 3LE, UK

Accepted 2020 August 11. Received 2020 July 17; in original form 2020 February 10

## ABSTRACT

We investigate the dependence of the galaxy properties on cosmic web environments using the most up-to-date hydrodynamic simulation: Evolution and Assembly of Galaxies and their Environments (EAGLE). The baryon fractions in haloes and the amplitudes of the galaxy luminosity function decrease going from knots to filaments to sheets to voids. Interestingly, the value of  $L^*$  varies dramatically in different cosmic web environments. At  $z = 0$ , we find a characteristic halo mass of  $10^{12} h^{-1} M_{\odot}$ , below which the stellar-to-halo mass ratio is higher in knots, while above which it reverses. This particular halo mass corresponds to a characteristic stellar mass of  $1.8 \times 10^{10} h^{-1} M_{\odot}$ . Below the characteristic stellar mass, central galaxies have redder colours, lower sSFRs, and higher metallicities in knots than those in filaments, sheets and voids, while above this characteristic stellar mass, the cosmic web environmental dependences either reverse or vanish. Such dependences can be attributed to the fact that the active galaxy fraction decreases along voids, sheets, filaments, and knots. The cosmic web dependences get weaker towards higher redshifts for most of the explored galaxy properties and scaling relations, except for the gas metallicity versus stellar mass relation.

**Key words:** galaxies: evolution – galaxies: general – large-scale structure of Universe.

## 1 INTRODUCTION

The large-scale structure (LSS) of the Universe exhibits a web-like structure, which is usually categorized into four components: voids, sheets, filaments, and knots. It originates from small perturbations in the very early Universe and is shaped gradually by the large-scale gravitational fields. Different components correspond to different stages of gravitational collapse. Large sheets of matter form via gravitational collapse along one principal direction, filaments form via gravitational collapse along two principal axes, and knots form via gravitational collapse along three principal axes. The relatively empty regions of the Universe between knots, filaments, and sheets are referred to as cosmic voids, whose density is well below the cosmic mean value. Most mass is contained in knots and filaments, while most volume is filled by voids. The relative mass fractions and filling factors of each component could evolve significantly from high to low redshifts (Zhu & Feng 2017; Cui et al. 2019).

The cosmic web environments have influences on the halo formation history and the halo properties. Haloes in knots tend to be older than those in other web environments and massive haloes in knots have higher spin than those in filaments, sheets, and voids (e.g. Hahn et al. 2007). The halo mass function strongly depends on the web environment such that it has a much higher amplitude in filaments than in voids (e.g. Ganeshaiah Veena et al. 2018). Recently, the large-scale cosmic web environment was also found to correlate

with the orientation of haloes (e.g. Zhang et al. 2009; Codis et al. 2012; Ganeshaiah Veena et al. 2018). However, the role the cosmic web plays in galaxy formation is not clear. Recent work found that the blue galaxy fraction and the star formation rate (SFR) of blue galaxies decline from the field to knots at low redshift, but the dependence disappears at higher redshifts (Darvish et al. 2017; Kraljic et al. 2018). Similar trends are also found in the state-of-the-art hydrodynamical simulation HORIZON-AGN (Dubois et al. 2014). Using the Sloan Digital Survey (SDSS), Chen et al. (2017) demonstrated that red, massive galaxies tend to reside in filaments more than blue, less-massive galaxies.

It has been suggested that the cosmic web shapes the galaxy properties primarily through the strong dependence of the galaxy properties on the mass of their host halo (e.g. Gay et al. 2010; Yan, Fan & White 2013; Goh et al. 2019). This is also supported by Eardley et al. (2015), who found in Galaxy And Mass Assembly survey (GAMA) that the strong variation of galaxy properties in different cosmic web structures vanishes when comparing at the same local density. However, by using SDSS data, Poudel et al. (2017) found that at a fixed halo mass, central galaxies in filaments have redder colours, higher stellar mass, lower specific star formation rates (sSFRs), and higher abundances of elliptical galaxies compared to those outside the filaments. Observationally, it is hard to measure the halo mass for an individual galaxy, while stacking methods could smear out the cosmic web dependence if it is not strong enough. Theoretical work, using cosmological hydrodynamical simulations, can provide more clues to such studies. Using IllustrisTNG, Martizzi et al. (2020) found at a given halo mass, galaxies with stellar masses lower than the median value are more likely to be found in voids and

★ E-mail: guoqi@nao.cas.cn

sheets, whereas galaxies with stellar masses higher than the median are more likely to be found in filaments and knots. Liao & Gao (2019) found that haloes in filament have higher baryon fractions and stellar mass fractions compared to those in the field.

In recent years, cosmological hydrodynamical simulations have gained great success in reproducing many observed galaxy properties (e.g. Vogelsberger et al. 2014; Schaye et al. 2015). In such simulations, the cosmic web effect is taken into account automatically. Here, we use the state-of-art cosmological hydrodynamical simulation, Evolution and Assembly of Galaxies and their Environments (EAGLE) to disentangle the connections between galaxies, dark matter haloes, and the cosmic web and revisit the relation between galaxy properties and geometric cosmic web structures.

This paper is organized as follows. We introduce the EAGLE simulation and describe the environmental classification method in Section 2. The cosmic-web dependence of the various baryonic components and the scaling relations are presented in Sections 3 and 4, respectively. In Section 5, we summarize our results.

## 2 SIMULATION AND METHODS

### 2.1 EAGLE simulation

The EAGLE simulation consists of a series of cosmological simulations performed with a modified version of the N-body Tree-PM smoothed particle hydrodynamics (SPH) code GADGET-3 (Springel 2005). In this paper, we use the largest volume EAGLE simulation, labelled as L100N1504, which was carried out in a box of 100 Mpc each side, tracing  $1504^3$  dark matter particles and an equal number of baryonic particles. The initial mass of the gas particles is  $1.81 \times 10^6 M_\odot$  and the dark matter particles mass is  $9.70 \times 10^6 M_\odot$ . The EAGLE simulations adopt the cosmological parameters taken from the Planck results (Planck Collaboration I, 2014):  $\Omega_m = 0.307$ ,  $\Omega_\Lambda = 0.693$ ,  $\Omega_b = 0.04825$ ,  $h = 0.6777$ ,  $\sigma_8 = 0.8288$ ,  $n_s = 0.9611$ , and  $Y = 0.248$ .

The simulations used state-of-art numerical techniques and sub-grid physics including radiative cooling and photoheating (Wiersma, Schaye & Smith 2009a), star formation law (Schaye & Dalla Vecchia 2008), stellar evolution and enrichment (Wiersma et al. 2009b), stellar feedback (Dalla Vecchia & Schaye 2012), and black hole seeding and growth (Springel, Di Matteo & Hernquist 2005; Rosas-Guevara et al. 2015). These models were proven successful in reproducing many observed galaxy properties including the galaxy stellar mass function, galaxy sizes, and the amplitude of the galaxy-central black hole mass relation, etc. (Schaye et al. 2015). The friends-of-friends (FOF) method (Davis et al. 1985) was performed on the particle data to generate FOF groups by linking particles separated by 0.2 times the average particle separation. In each FOF group, the SUBFIND (Springel et al. 2001; Dolag et al. 2009) algorithm was applied to identify the self-bound particles as subhalos/substructures.  $M_{200}$  is adopted to refer to the virial mass, which is the total mass within  $R_{200}$  within which the average density is 200 times the critical density. Galaxies reside in the centre of each substructure. The stellar mass is defined as the total mass of stellar particles within 30 pkpc radii of the centre of each subhalo. The luminosity and colour are calculated using a stellar population synthesis model taking into account the SFR history and metallicity of each star particle (Trayford et al. 2015). In the public EAGLE simulation catalogue, it provides magnitudes in the five rest-frame SDSS bands and 3 UKIRT bands. This sample contains absolute rest-frame magnitudes for all galaxies with  $M_* > 10^{8.5} M_\odot$ . No dust attenuation has been included.

### 2.2 Environmental classification

The cosmic web presents itself in large-scale surveys, as well as in cosmological simulations. Many different approaches to classify the cosmic web elements have been developed in the literature. The tidal tensor and the velocity shear tensor are two of the most popular quantities to identify the cosmic web (see Libeskind et al. 2018 for a comparison of different classifications of the cosmic web). Here, we follow Hahn et al. (2007) to use the tidal tensor to classify the four cosmic web elements.

A region is identified as void, sheet, filament, or knot according to the number of dimensions that this particular patch collapses along. The tidal tensor  $T_{ij}$  is given by the Hessian matrix of the gravitational potential  $\phi$

$$T_{ij} = \frac{\partial^2 \phi}{\partial r_i \partial r_j}. \quad (1)$$

The gravitational potential  $\phi$  from the matter density field is obtained using the Poisson's equation

$$\nabla^2 \phi = \delta, \quad (2)$$

where  $\bar{\rho}$  denotes the mean mass density of the universe and  $\delta = \frac{\rho}{\bar{\rho}} - 1$  denotes the density contrast. In practice, we split the simulation box into  $256^3$  Cartesian cells and estimate the density and density contrast by assigning the particles to each cell using the cloud-in-cell method (Sefusatti et al. 2016). We further smooth the discrete density field with a Gaussian filter of width  $R_s = 1.25 \text{ Mpc h}^{-1}$ .

There are three eigenvalues of the tidal tensor  $T_{i,j}$ ,  $\lambda_1 \geq \lambda_2 \geq \lambda_3$ . Hahn et al. (2007) used the number of positive eigenvalues of  $T_{ij}$  ( $\lambda_{th} = 0$ ) to classify the four possible environments. However, in reality, such criteria lead to an underestimate of the filling factor of the voids. We follow Forero-Romero et al. (2009) to introduce an eigenvalue threshold  $\lambda_{th}$ , as a free parameter and define the cosmic web elements as following:

- (i) Void: all eigenvalues  $\lambda_i$  below the threshold  $\lambda_{th}$  ( $\lambda_{th} \geq \lambda_1 \geq \lambda_2 \geq \lambda_3$ ).
- (ii) Sheets: two eigenvalues  $\lambda_i$  below the threshold  $\lambda_{th}$  ( $\lambda_1 \geq \lambda_{th} \geq \lambda_2 \geq \lambda_3$ ).
- (iii) Filaments: one eigenvalues  $\lambda_i$  below the threshold  $\lambda_{th}$  ( $\lambda_1 \geq \lambda_{th} \geq \lambda_2 \geq \lambda_3$ ).
- (iv) Knots: all eigenvalues  $\lambda_i$  above the threshold ( $\lambda_1 \geq \lambda_2 \geq \lambda_3 \geq \lambda_{th}$ ).

Here, we adopt a fixed  $\lambda_{th} = 0.25$  at  $z = 0, 1, 3.01, 5.97$ . We test our results using different  $\lambda_{th}$  at different redshifts and find the results are in qualitative agreement with those with the fixed  $\lambda_{th}$ . This is consistent with the conclusions reached by Zhu & Feng (2017). In Fig. 1, we show the map of the overdensity and the corresponding cosmic web in a slice  $0.265 \text{ Mpc h}^{-1}$  thick at  $z = 0$ . The cosmic structures are well captured by the tidal tensor method.

## 3 BARYONIC PROPERTIES IN THE COSMIC WEB

### 3.1 Total baryons

Table 1 summarizes the volume fractions and mass fractions in different cosmic web environments. At  $z = 0$ , the volume fractions are 0.407, 0.416, 0.168, and 0.010 among the void, sheets, filaments, and knots, while the total mass fractions located in each structure element are 0.089, 0.239, 0.392, and 0.279. This is consistent with the results using Illustris simulation that most matter resides either in haloes or in filaments but very little in voids, though the voids

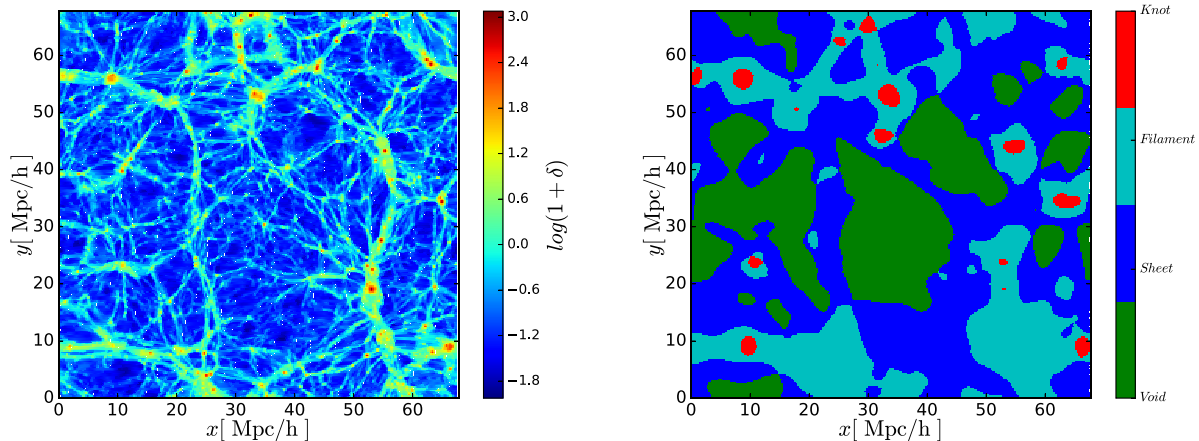


**Figure 1.** Left-hand panel: Overdensity map of a slice of  $0.265 \text{ Mpc h}^{-1}$  thickness. The colour bar denotes the values of logarithm of the overdensity. Right-hand panel: The corresponding cosmic web elements generated using the method as described in Section 2.2. Red, cyan, blue, and green regions are for the knots, filaments, sheets, and voids, respectively.

**Table 1.** Volume fraction and mass fraction in each cosmic web component in the EAGLE simulations at  $z \sim 0, 1, 3, 6$ . Columns 1: redshifts; Columns 2, 3, 4, 5: volume fraction in knots, filaments, sheets and voids, respectively; Columns 6, 7, 8, 9: mass fraction in knots, filaments, sheets, and voids, respectively (numbers within brackets are for baryonic mass fraction only).

Redshift	Volume fraction				Mass fraction			
	Knot	Filament	Sheet	Void	Knot	Filament	Sheet	Void
0	0.010	0.168	0.416	0.406	0.279(0.268)	0.393(0.398)	0.239(0.244)	0.089(0.090)
1	0.010	0.138	0.397	0.455	0.154(0.147)	0.355(0.358)	0.329(0.332)	0.162(0.163)
3	0.007	0.083	0.331	0.579	0.042(0.042)	0.209(0.209)	0.392(0.392)	0.357(0.357)
6	0.001	0.024	0.187	0.788	0.004(0.004)	0.057(0.057)	0.272(0.272)	0.667(0.667)

contribute a significant fraction of the total volume (Haider et al. 2016). Both the volume fraction and mass fraction of voids increase with redshift, whilst they decrease in knots and filaments.

For the baryon component, as expected, it is a good tracer of the total matter at large scales across cosmic time (Cen & Ostriker 1999; Davé et al. 2001; Eckert et al. 2015). We find that the baryon fraction in knots and filaments decreases dramatically with redshifts. Cui et al. (2019) reached similar conclusions as ours, though their classification of the cosmic web adopted a different cell size and eigenvalue threshold, indicating our results are qualitatively robust against the method of classification of the cosmic web. In addition, Cui et al. (2019) demonstrated that the baryon fraction in different components of the web and its evolution depend only very weakly on the different physics implemented in the simulations.

We further investigate the normalized baryon fraction ( $f_{\text{bar}}/\bar{f} = (M_{\text{bar}}/M_{200\text{crit}})/(\Omega_b/\Omega_0)$ ) as a function of halo mass in different cosmic web environments (Fig. 2), where  $\bar{f}$  is the universal baryonic fraction 15.7 per cent,  $f_{\text{bar}}$  is the baryon fraction measured within  $R_{200}$ . It shows that the baryonic fraction is an increasing function of the halo mass in all web environments. The strong halo mass dependence of the baryonic fraction presents itself over all the redshifts from 0 to 6. At  $z = 0$ , only in massive clusters ( $\sim 10^{14} h^{-1} M_{\odot}$ ), the baryonic fraction does reach the universal value, while this fraction drops dramatically towards lower masses. At low masses, the overall baryonic fraction increases significantly with redshifts. For example, for haloes of  $M_{200\text{crit}} \sim 10^{10} h^{-1} M_{\odot}$ , the baryon fraction increases from 0.1 at  $z \sim 0$  to 0.4 at  $z \sim 5.97$ . In the MassiveBlack-II simulation, Khandai et al. (2015) found an even stronger redshift evolution of the baryon fraction. Peirani et al. (2012) found a similar

trend of the mean baryonic fraction in groups over cosmic time using hydrodynamical zoom-in simulations. They claimed that it is due to the lower accretion rate of dissipative gas on to the haloes compared to that of dark matter at low redshifts. Another reason for the high baryon fraction at high redshifts is that the potential well is deeper and it is, thus, harder to expel baryons out even for haloes of relatively low masses. On the other hand, for the massive systems (more massive than  $10^{13} h^{-1} M_{\odot}$ ), their baryonic fractions hardly change with redshifts. Haloes of such masses have potential wells deep enough to keep most of their baryons both at low and at high redshifts.

The baryonic fraction increases from voids, sheets, filaments towards knots. For haloes of  $10^{11} h^{-1} M_{\odot}$ , the baryonic fraction in voids is lower than that in knots by 0.8 dex at  $z = 0$ . It is much stronger dependence than that found by Metuki et al. (2015), who used simulations with different subgrid physics. This cosmic web dependence gets weaker towards lower masses and almost vanishes at  $10^{10} h^{-1} M_{\odot}$ . Fig. 2 also shows that, in general, the cosmic web dependence gets stronger with redshifts up to  $z = 3$ , especially at low masses. At the highest redshift,  $z \sim 6$ , the cosmic web dependence gets weaker again.

### 3.2 Stellar mass-to-halo mass ratios

In this section, we focus on the stellar mass and its relation to the cosmic web. The cosmic web dependences of the galaxy properties versus stellar masses relations are presented in Section 4.

We show the stellar mass-to-halo mass ratio for central galaxies ( $M_{\star, \text{central}}/M_{200\text{crit}}$ ) at various redshifts in Fig. 3. As presented by

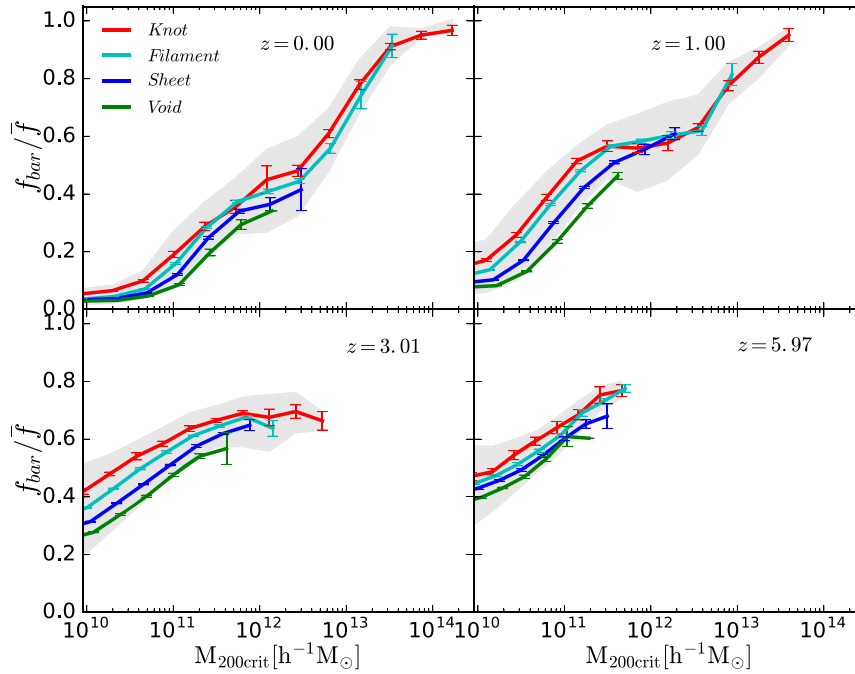


**Figure 2.** Baryon fraction as a function of halo mass in different cosmic web environments. The shaded regions indicate the 16–84th percentile scatter in each corresponding halo mass bin. Red, cyan, blue, and green curves denote the median values of the baryonic fractions in knots, filaments, sheets, and voids, respectively. Error bars present errors on the median values estimated based on 1000 bootstrap samples. Redshifts are indicated on the top right-hand corner of each panel.

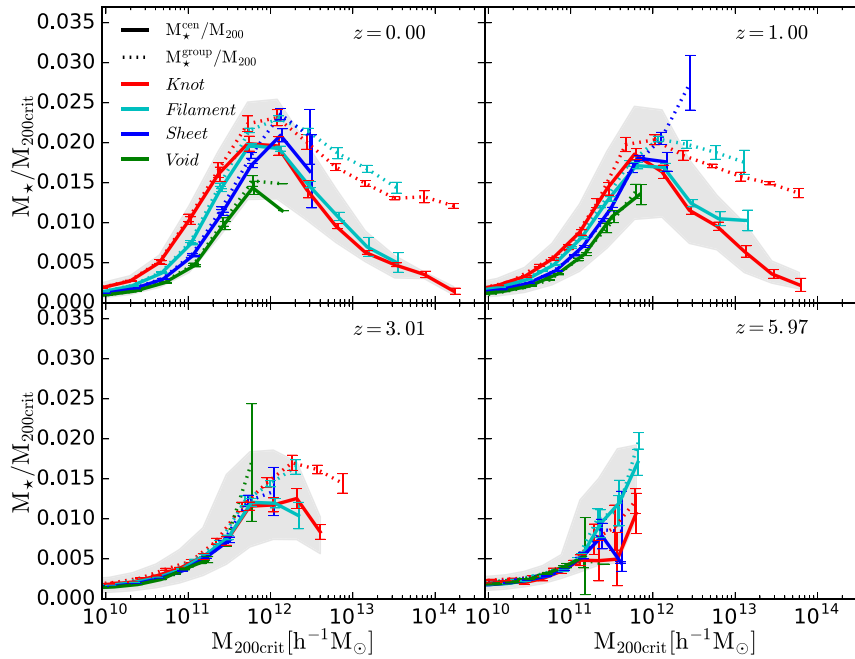


**Figure 3.** Stellar mass-to-halo mass relation as a function of cosmic web environments. The solid curves account for stellar mass in central galaxies while the dashed curves account for the total stellar mass within the corresponding virial radius. The shaded regions indicate the 16–84th percentile scatter in each corresponding halo mass bin. Red, cyan, blue, and green curves denote the median values of the ratios in knots, filaments, sheets, and voids, respectively. Errors are estimated based on 1000 bootstrap samples. Redshifts are indicated on the top right-hand corner of each panel.

Schaye et al. (2015), the trend of the full sample is consistent with that inferred by the subhalo abundance matching methods (e.g. Guo et al. 2011; Moster, Naab & White 2013) at  $z = 0$ . A similar analysis is applied to the total stellar mass fraction ( $M_{\star, \text{group}}/M_{200\text{crit}}$ , dotted

curves), where the total stellar mass referred to is the total stellar masses within  $R_{200}$ . It peaks at  $\sim 10^{12} h^{-1} M_{\odot}$  and drops fast both towards the low mass and high mass ends. Different from the stellar-to-halo mass ratio for central galaxies, the slope at high masses is



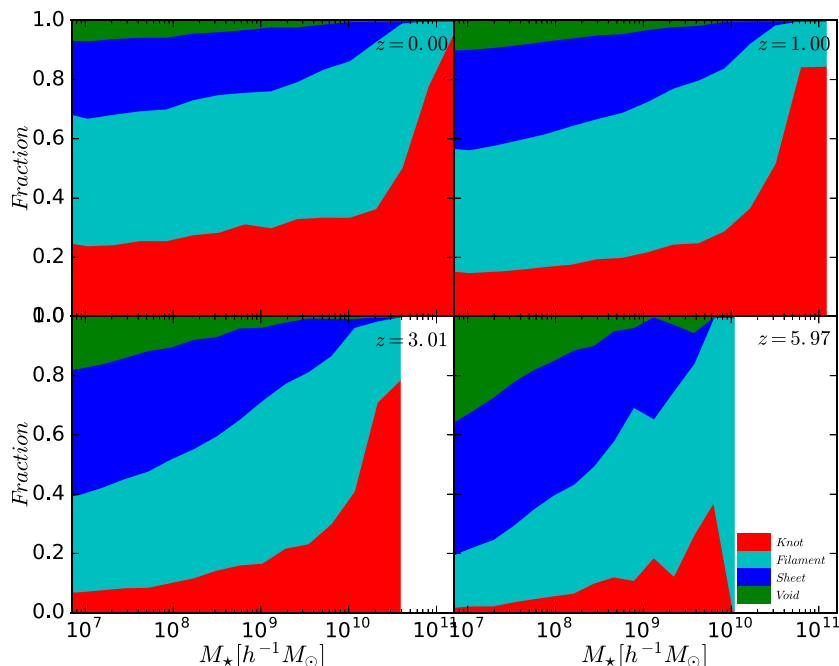


**Figure 4.** Fractions of galaxies in different web environments as a function of stellar mass at  $z \sim 0, 1, 3.01$ , and  $5.97$ . Red, cyan, blue, and green regions represent the fractions in knots, filaments, sheets, and voids, respectively. Redshifts are indicated at the top right-hand corner of each panel.

much flatter for the total stellar masses. At low masses, the central and total stellar mass-to-halo mass ratios are almost identical, indicating that satellite galaxies and intra-cluster lights contribute more to massive systems than to low mass systems. These trends are found at redshifts up to  $z \sim 3$ . At  $z = 6$ , no high-mass systems are formed due to the limited box size. The amplitudes of the central and total stellar-to-halo mass ratios decrease towards higher redshifts, consistent with the finding from the subhalo abundance matching method (Moster et al. 2013) that the galaxy formation efficiency decreases slightly with increasing redshifts.

At  $z = 0$ , the central and total stellar mass-to-halo mass ratios decrease from knots to filaments to sheets and to voids for haloes below  $\sim 10^{12} h^{-1} M_{\odot}$ . In haloes of  $10^{11} h^{-1} M_{\odot}$ , where most of the dwarf galaxies reside, the ratios drop by a factor of  $\sim 2$ . At high masses, it is the opposite. In knots, the ratios are the lowest while in voids the ratios are the highest. At the peak location ( $\sim 10^{12} h^{-1} M_{\odot}$ ), about the mass of the Milky Way’s halo, the central and total stellar mass-to-halo mass ratios do not vary between different cosmic web environments. Such environmental dependencies are also found at  $z = 1$ , though somehow weaker than that at  $z = 0$ . At even higher redshifts ( $z > 3$ ), the cosmic web dependence vanishes at low masses and no statistical results can be obtained at high masses due to the limited number of high-mass systems.

### 3.3 Stellar mass functions

Most stars are locked in galaxies. The fraction of galaxies as a function of stellar mass in different cosmic web environments are shown in Fig. 4. In a given stellar mass bin, the fraction of galaxies in any cosmic web environment is calculated by dividing the number of galaxies in the corresponding web environment by the total number of galaxies. In the top left-hand panel, it shows that at  $z = 0$ , most of the massive galaxies reside in knots, consistent with previous results (Eardley et al. 2015; Metuki et al. 2015). For galaxies of

the Milky Way mass and dwarf galaxies, most reside in filaments, though a comparable, yet slightly lower fraction reside in knots. This is also found by Eardley et al. (2015) using GAMA data and Metuki et al. (2015) using simulations. Only a very small fraction of galaxies reside in voids at all masses considered here. The fractions in different cosmic web environments are similar at  $z = 1$ . At higher redshifts, more galaxies are found in voids and sheets than at lower redshifts, while less is found in knots and filaments, especially at low masses.

The dependence on the cosmic web is more significant when converting the total number of galaxies to the volume number density (the stellar mass functions) as shown in Fig. 5. At  $z = 0$ , the number density drops by two orders of magnitude from knots to voids. Such strong dependencies are also found by theoretical work (Metuki et al. 2015) and observational work (Alpaslan et al. 2015). Interestingly, we find the mass at the knee (corresponding to  $L^*$ ) decreases by a factor of  $\sim 8$ , with the value of  $10^{10.8} h^{-1} M_{\odot}$  in the knots and  $10^{10.0} h^{-1} M_{\odot}$  in voids. This change is dramatic given that the corresponding mass for the global stellar mass function barely changes since  $z \sim 1$  (e.g. Beare et al. 2019). As for the number fractions, the cosmic web environmental dependence of the stellar mass functions gets weaker at high redshifts. The evolution is stronger at low masses than that at high masses.

## 4 SCALING RELATIONS IN THE COSMIC WEB

The observed scaling relations are very important in revealing the underlying physics of galaxy formation. In this section, we show how cosmic web environments affect the colour versus stellar mass relation, sSFR versus stellar mass relation and stellar/gas metallicity versus stellar mass relation. Since the environmental dependence of satellite galaxies are very much different from that of central galaxies (e.g. Peng et al. 2010), in this section we focus on *central* galaxies only.

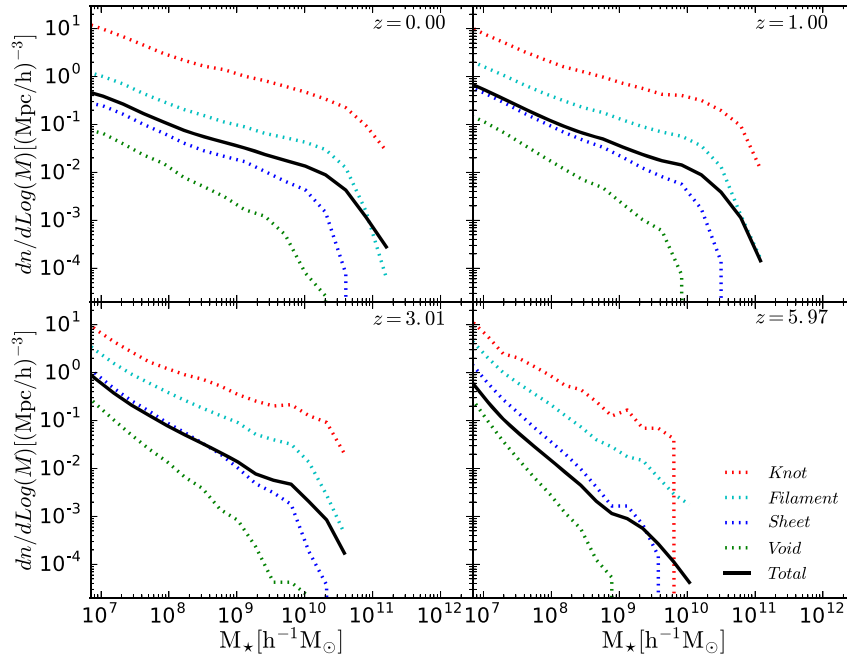


**Figure 5.** The stellar mass functions in different cosmic web environments at different redshifts. Solid black curves are the overall stellar mass functions, while dashed ones are those for different environments with the same colour coding as those in Fig. 4.

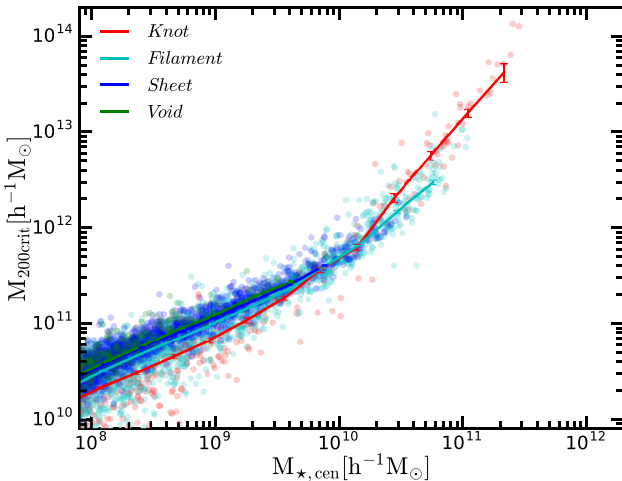


**Figure 6.** The halo mass versus stellar mass relation for central galaxies at  $z = 0$ . The shaded regions indicate the 16–84th percentile scatter in each corresponding stellar mass bin. Red, cyan, blue, and green curves denote the median value of the ratios in knots, filaments, sheets, and voids, respectively. Error bars are generated using the bootstrap method.

Previous work found that the cosmic web dependence and the halo mass dependence are highly degenerate (e.g. Brouwer et al. 2016). Large-scale web environments could shape the galaxy properties through the halo mass for galaxies properties which depend strongly on halo mass (e.g. Metuki et al. 2015) and LSSs affect halo masses significantly. We show in Fig. 6 that for a given stellar mass, the typical halo mass varies in different cosmic environments. For galaxies with stellar mass below  $1.8 \times 10^{10} h^{-1} M_{\odot}$ , the host haloes are less massive in knots, while for those with stellar mass above  $1.8 \times 10^{10} h^{-1} M_{\odot}$ , the host haloes are more massive in knots. This is consistent with what we found in Fig. 3. In order to disentangle

the connections between the cosmic web, dark matter haloes and galaxies, we measure the *pure* cosmic environmental effects by removing the dark halo effects. In practice, for any quantity of interest,  $X$ , we calculate  $R_X$  as a function of the cosmic web environment, where  $R_X$  is defined as

$$R_X = \frac{X}{\langle X | M_{200\text{crit}} \rangle} - 1. \quad (3)$$

For each  $M_{200\text{crit}}$  at a given redshift, we calculate the average value of  $X$ ,  $\langle X | M_{200\text{crit}} \rangle$ , in advance.  $R_X$  quantifies the off-set of the property  $X$  that deviates from the expected values for given halo masses.

For any quantity  $X$  that depends directly only on halo mass, the mean of  $R_X$  will equal 0 for any subsample, including one defined by stellar mass and environment, as below. By using  $R_X$ , we can test whether an apparent dependence of  $X$  on environment at a given stellar mass is entirely driven by the dependence of halo mass on environment at given stellar mass or whether there is some remaining dependence on environment at fixed halo mass.

#### 4.1 Colour versus stellar mass

Colour is one of the most important observables for it is key to understand galaxies' star formation history. Previous studies found that galaxies on the colour versus stellar mass diagram can be grouped into three categories, blue cloud (active), red sequence (passive), and green valley (those in between). Galaxies in low-density environments (e.g. filaments, sheets, and voids) tend to be bluer, while those in high-density environments (knots) tend to be redder (Poudel et al. 2017). However, this could be caused by the fact that in low density regions, galaxies and their host haloes are smaller, while smaller galaxies are, in general, bluer (Baldry et al. 2006; Cucciati, Iovino & Kovač 2011).

Fig. 7 shows the  $g - r$  colour versus stellar mass relation as a function of the environments and stellar mass. Observed colours can be influenced by dust extinction and we, thus, use the intrinsic

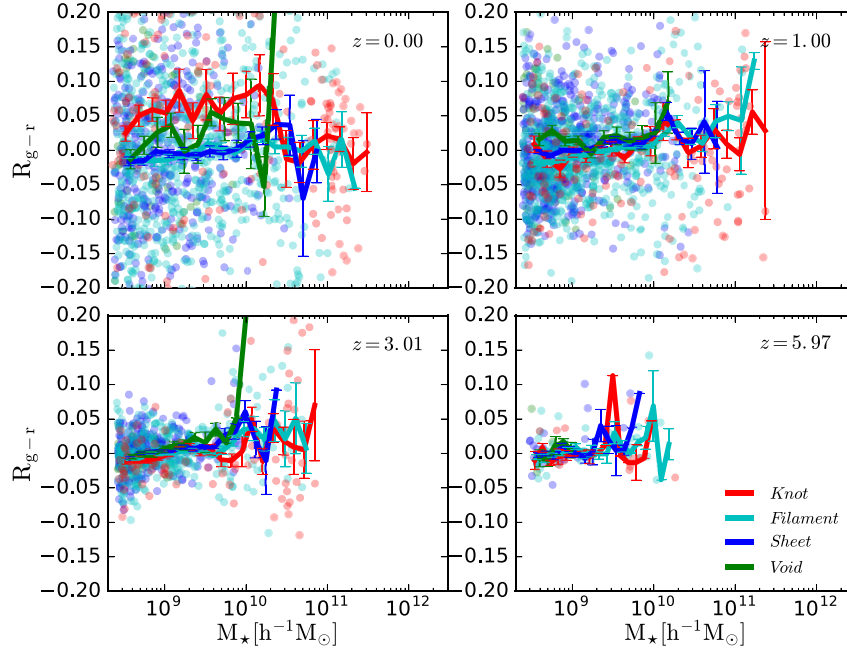


**Figure 7.** The deviation of  $g - r$  colour from the expected values as a function of stellar mass for central galaxies in different environments. Red, cyan, blue, and green curves denote the median value of the deviation in knots, filaments, sheets, and voids, respectively. Scatters are for each galaxy with the same colour coding as the curves. Error bars are generated using the bootstrap method. Redshifts are indicated at the top right-hand corner of each panel.

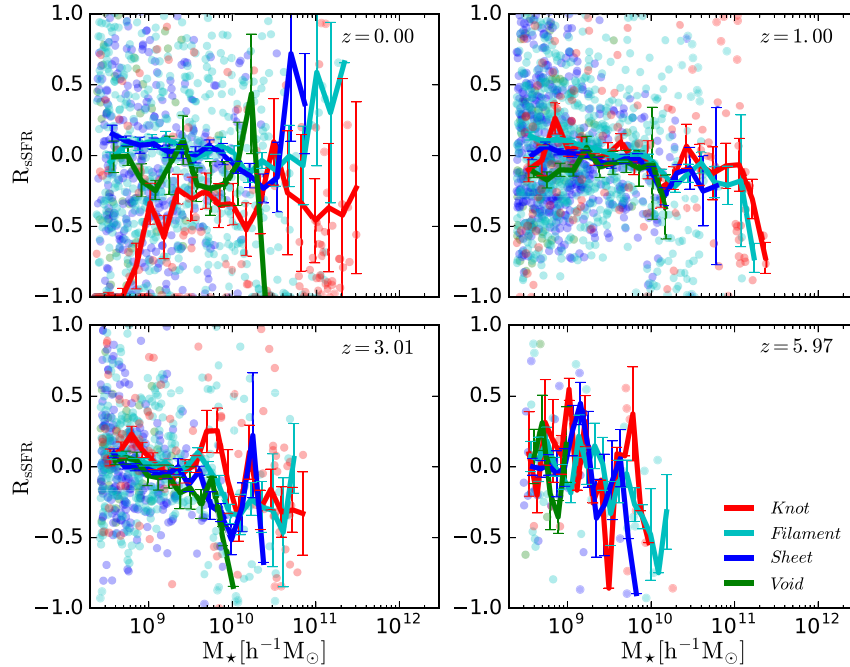


**Figure 8.** The deviation of specific star formation rate from the expected values as a function of stellar mass for central galaxies in different environments. Red, cyan, blue, and green curves denote the median value of the deviation in knots, filaments, sheets, and voids, respectively. Scatters are for each galaxy with the same colour coding as the curves. Error bars are generated using the bootstrap method. Redshifts are indicated at the top right-hand corner of each panel.

colour. For the colour is a dimensionless quantity and can be zero in many cases, instead of using equation (3) we adopt a slightly different quantity to remove the halo dependence. For each galaxy, we calculate  $R_{g-r} = (g - r) - \langle (g - r) | M_{200\text{crit}} \rangle$ . At  $z = 0$ , for galaxies less massive than  $1.8 \times 10^{10} h^{-1} M_{\odot}$ , it shows a clear dependence on

environments, especially for those in knots. Galaxies in knots are redder than those in voids by 0.08 mag ( $1.8\sigma$ ). This is related to the fraction of active galaxies in different environments which we will discuss, in more detail, in the next subsection. At stellar masses above  $1.8 \times 10^{10} h^{-1} M_{\odot}$ , there is no clear cosmic web environmental



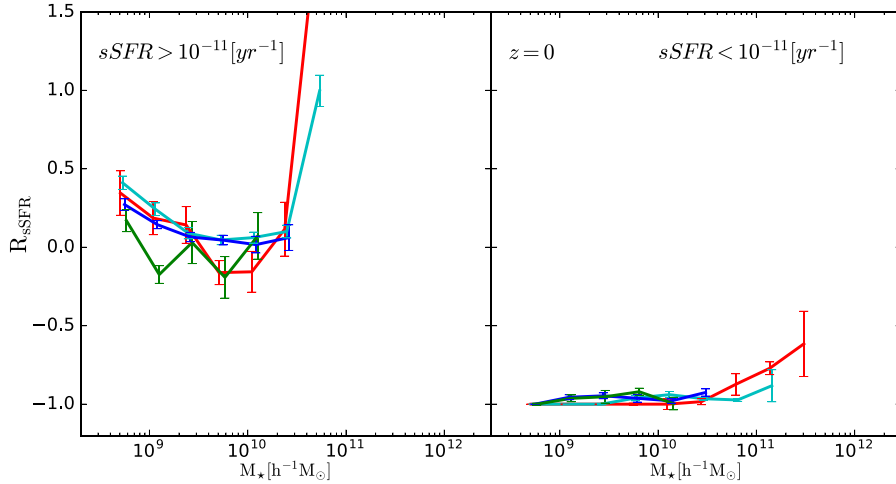


**Figure 9.** The deviation of the sSFR from the expected values as a function of stellar mass in different environments for active ( $sSFR > 10^{-11} \text{ yr}^{-1}$ , left-hand panel) and passive ( $sSFR < 10^{-11} \text{ yr}^{-1}$ , right-hand panel) galaxies at  $z=0$ . Red, cyan, blue, and green curves denote the median value of the deviation in knots, filaments, sheets, and voids, respectively. Error bars are generated using the bootstrap method.

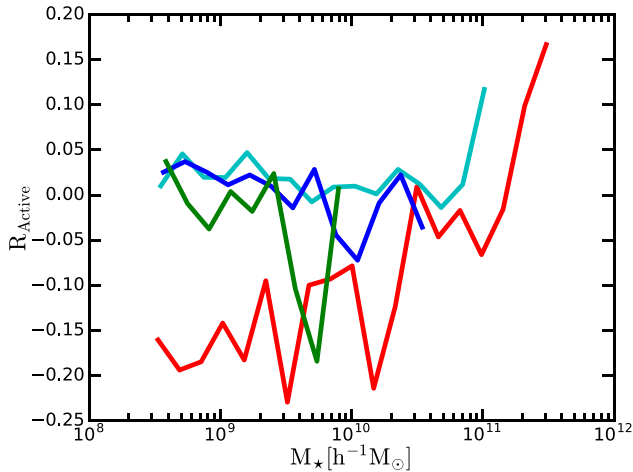


**Figure 10.** The deviation of active fraction from the expected values as a function of stellar mass for central galaxies in different environments at  $z=0$ . Red, cyan, blue, and green curves are for the knots, filaments, sheets, and voids, respectively.

dependence. The difference between voids and sheets is weak across all the stellar mass ranges.

The dependence on environments vanishes for galaxies at high redshifts:  $z = 1, 3$ , and  $6$  at all masses. This is consistent with Darvish et al. (2017), who found no cosmic web dependence of galaxy colour in the COSMOS fields at  $z = 1$ .

#### 4.2 Specific star formation rate versus stellar mass

Colours are influenced by the star formation history, especially the current SFR. Fig. 8 shows the sSFR as a function of stellar mass and cosmic environments. Similar to the colour versus stellar mass relation, at  $z = 0$ , the cosmic environmental dependence is the strongest for galaxies with stellar mass less than  $1.8 \times 10^{10} h^{-1} M_{\odot}$ . The sSFR is lower by 50 per cent in knots than that in voids. At higher masses, given the large scatters, we can not find clear environmental dependence. This is consistent with the observational

results by Poudel et al. (2017), who found central galaxies in low-density environments with higher sSFR compared to those in high-density environments at a fixed group mass using group catalogues (Tempel et al. 2014) extracted from the SDSS DR10. The cosmic environmental dependence is much weaker at high redshifts, broadly consistent with the results of Scoville et al. (2013) and Darvish et al. (2016). Different from the colour versus stellar mass relation, at  $z = 3$ , the sSFR is slightly higher in knots compared to that in other environments.

Corresponding to the red sequence and blue cloud, galaxies can be separated into passive and active sub-populations using their sSFRs. Unlike galaxy colours, sSFR is not affected by metallicity and star formation history. Here, we adopt  $\log(sSFR[\text{yr}^{-1}]) = -11$  as the threshold: galaxies with  $\log(sSFR[\text{yr}^{-1}]) < -11$  are referred to as passive galaxies, while those with  $\log(sSFR[\text{yr}^{-1}]) > -11$  are taken to be active (star-forming) galaxies. The threshold value is fixed over cosmic time as its evolution is not very strong (Matthee & Schaye 2019).

The left-hand panel in Fig. 9 shows the environmental dependence of the sSFR for active galaxies at  $z = 0$ . For active galaxies, no environmental dependences present themselves except for those with masses  $\sim 2.8 \times 10^9 h^{-1} M_{\odot}$ , where the sSFR of central galaxies is lower in voids than in other cosmic web environments. At higher masses, such dependence vanishes. For passive galaxies, as shown in the right-hand panel, there is no environmental dependence over all the stellar mass ranges considered.

The rather low sSFR in knots in the first panel of Fig. 8 might be explained by their low fraction of active galaxies. The average active galaxy fraction increases from knots, filaments to sheets and voids, ranging from 0.58, 0.81, 0.87, and 0.88, respectively. When taking into account the expected active galaxy fraction for any given halo mass and the number of haloes of the given mass in each cosmic web environment, the derived expected active galaxy fractions are 0.66, 0.78, 0.87, and 0.91 in knots, filaments, sheets, and voids, respectively. To make it more clear, we redo this analysis in each stellar mass bin and subtract the direct measurement of the active galaxy fraction from the correspondingly expected active galaxy fraction. The results are presented in Fig. 10. It shows that at masses below  $1.8 \times 10^{10} h^{-1} M_{\odot}$ , there are less active galaxies in knots than in filaments, sheets, and voids. It is the low fraction

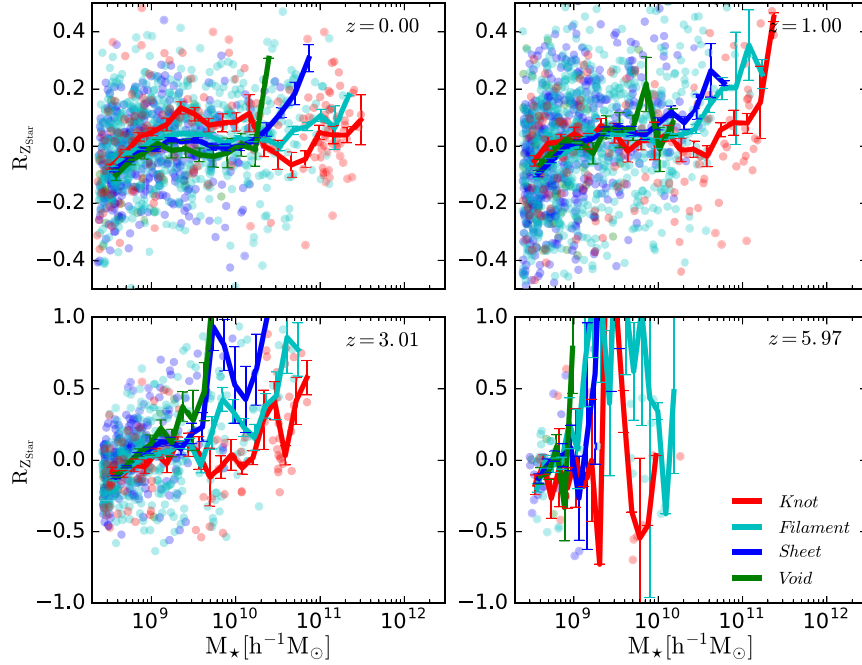


**Figure 11.** The deviation of the stellar metallicity from the expected values as a function of stellar mass for central galaxies in different environments. Red, cyan, blue, and green curves denote the median values of the deviation in knots, filaments, sheets, and voids, respectively. Scatters are for each galaxy with the same colour coding as the curves. Errors are generated using the bootstrap method. Redshifts are indicated at the top right-hand corner of each panel.

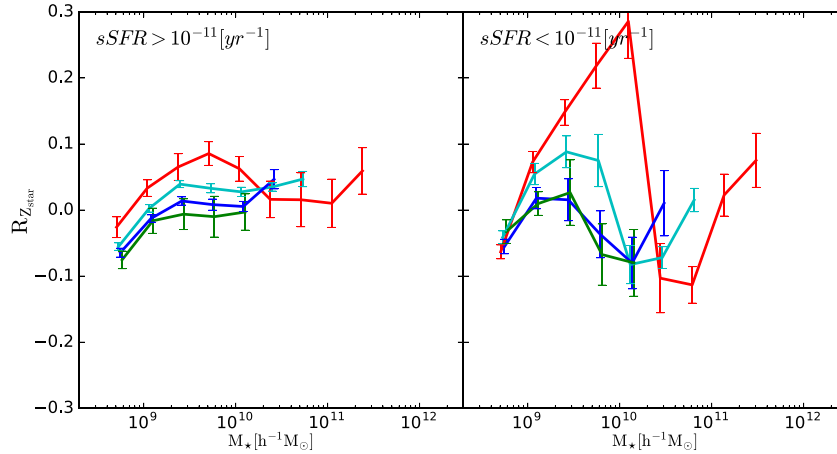


**Figure 12.** The deviation of the stellar metallicity from the expected values as a function of stellar mass in different environments for active (left-hand panel) and passive (right-hand panel) galaxies. Red, cyan, blue, and green curves denote the median values of the deviation in knots, filaments, sheets, and voids, respectively. Errors are generated using the bootstrap method.

of active galaxies in knots that leads to the low  $sSFR$  in knots. It also explains the redder colour in knots as shown in Fig. 7. Sobral et al. (2011) have also argued that the environment is responsible for star formation quenching in dense environments. In other words, denser environments increase the possibility of galaxies to become quenched. At high masses, on the other hand, there is instead not much difference in the active fraction in different environments. As a consequence, the cosmic web dependences of the colour and  $sSFR$  also vanish.

At high redshifts, most galaxies are star forming and there is almost no environmental dependence of the active fraction: at  $z >$

1, the active fraction approaches 1 in all cosmic web environments. The environmental dependence of the  $sSFR$  thus vanishes.

#### 4.3 Metallicity versus stellar mass

Metal enrichment is one of the most important processes in galaxy evolution which involves the gas cooling, star formation, supernova feedback, etc. Schaye et al. (2015) found the gas and stellar metallicity versus stellar mass relations in EAGLE are in broad agreement with observations for galaxies more massive than  $10^9 M_\odot$ , though at the low mass end the relations are not as steep as the observed ones.

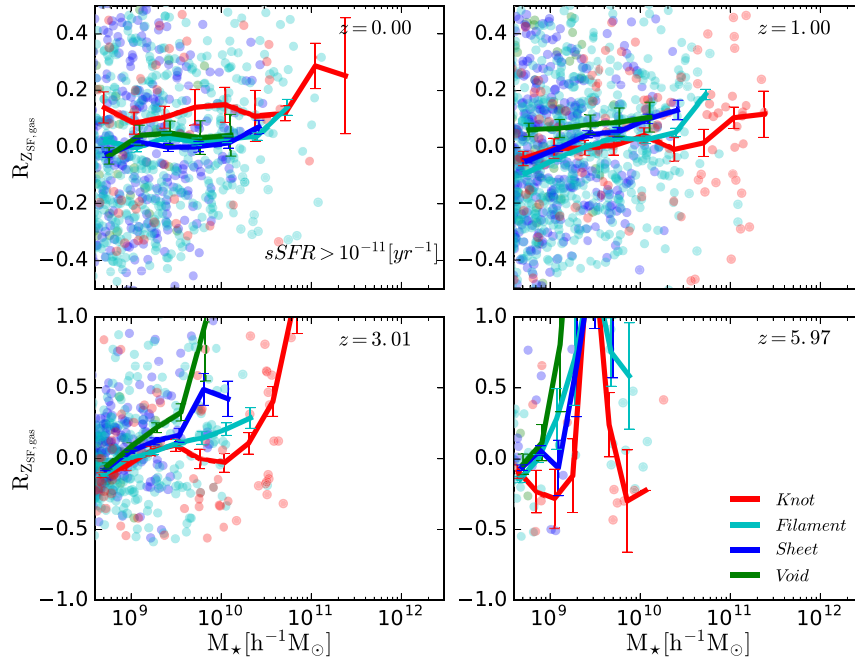


**Figure 13.** Similar to Fig. 11, but for gas metallicity of active galaxies.

Fig. 11 shows the stellar metallicity versus stellar mass relation in the different cosmic web environment. At low masses ( $M_* \sim 1.8 \times 10^{10} h^{-1} M_\odot$ ), the metallicity is higher in knots than in other environments. This is related to the relation between stellar mass, metallicity and SFR, as discovered in previous works (e.g. Ellison et al. 2008; Mannucci et al. 2010; Yates, Kauffmann & Guo 2012; De Rossi et al. 2015). Specifically, De Rossi et al. (2017) found that in EAGLE simulations the metallicity of low-mass systems decreases with SFR for a given stellar mass. The high metallicity in knots is thus consistent with their low SFRs as shown in Fig. 8. Such environmental dependence is much weaker at high redshifts.

Different from the relation with sSFR and colour, the stellar metallicity versus stellar mass relation shows a strong dependence on cosmic environments at high masses. The metallicity increases from knots, filaments, sheets towards voids. This is consistent with the increasing central stellar mass-to-halo mass ratios along knots, filaments, sheets, and voids, i.e. more metals are generated if more stars are formed. Such dependence persists up to  $z = 3$ . At even higher redshifts, there are not enough samples to make solid conclusions.

As for the sSFR, we split the galaxies into active and passive subsamples at  $z = 0$ . The transition mass at  $M_* \sim 1.8 \times 10^{10} h^{-1} M_\odot$  presents itself both for the active and passive galaxies, below which the metallicity is higher in knots, while above which the metallicity is lower in knots. The environmental dependence is stronger for passive galaxies than for active galaxies.

The cosmic web dependences of the gas metallicity as a function of stellar mass and redshift are presented in Fig. 13. Since there is very little gas in passive galaxies, here, we focus on active galaxies. At  $z = 0$ , at stellar masses below  $1.8 \times 10^{10} h^{-1} M_\odot$ , the gas metallicity is higher in knots, while at high masses, the difference between different web environments disappears. Different from other scaling relations, this cosmic web dependence of gas metallicity gets stronger at higher redshifts for massive galaxies. The gas metallicity is the lowest in knots and gets higher along filaments, sheets, and voids.

#### 4.4 Combined effects of cosmic web and dark matter haloes

We remove the halo effect from the cosmic web dependence in previous sections. However, it is difficult to obtain halo mass observationally. Here, we present the *apparent* cosmic web dependence (including halo effects, hereafter, we refer to it as combined dependence) on the scaling relations. Since the cosmic environmental effect is weak at high redshifts for most of the scaling relations, we focus on results at  $z = 0$ .

The top left-hand panel of Fig. 14 shows the  $g - r$  colour versus stellar mass relations for galaxies in different environments. Galaxies are redder in knots compared to other environments at all masses. This is different from the results shown in Fig. 7 that when removing halo effects at stellar mass above  $1.8 \times 10^{10} h^{-1} M_\odot$  galaxies in knots have similar colours as those in filaments, sheets, and voids. Such dependences are also found in the sSFR versus stellar mass relations (middle left-hand panel). These can be explained by the fact that there are more massive haloes in high density regions and galaxies in massive haloes are usually redder/with lower sSFR. The active fraction increases with stellar mass up to  $\sim 3 \times 10^9 h^{-1} M_\odot$  and decreases towards higher masses. This variations with stellar mass are similar to each other between voids, sheets, and filaments. For those in knots, the amplitude is lower, the turn-over mass is higher, and at low masses, the slope is steeper.

For a given stellar mass, the halo mass is lower in knots for those with stellar mass below  $1.8 \times 10^{10} h^{-1} M_\odot$  (Fig. 6). In low mass haloes, the feedback is usually more effective and it is, thus, easier for new formed heavy elements to escape. This compensates with the cosmic web dependence of stellar metallicity as shown in Fig. 11, resulting in the absence of variance between different environments as shown in top right-hand panel of Fig. 14. At high masses, the stellar metallicity decreases with environmental densities, similar to those without halo effects (Fig. 11). For the gas metallicity versus stellar mass relation (right-hand bottom panel of Fig. 14), there is almost no difference between voids, sheets, and filaments. On the other hand, the scaling relation in knots is very different. It increases rapidly with

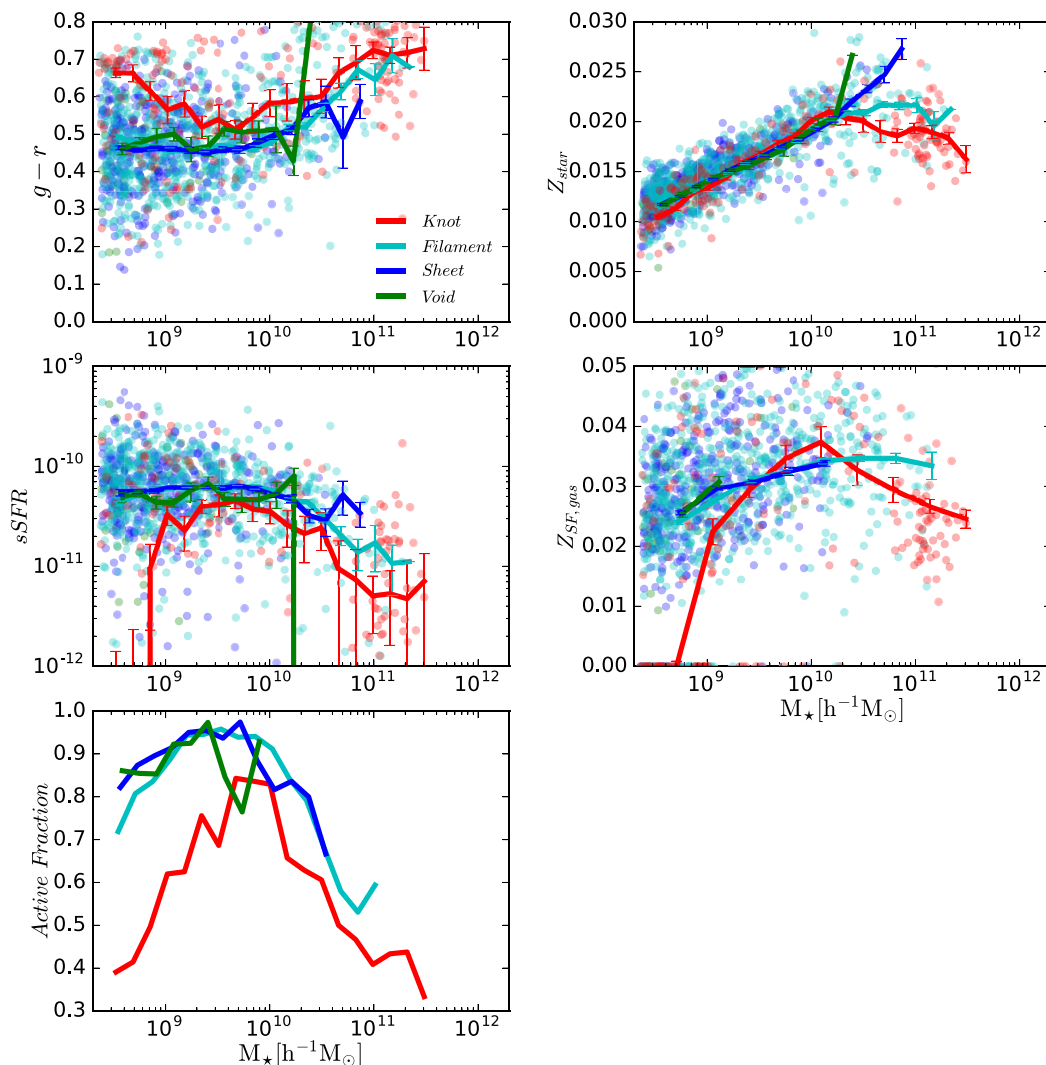


**Figure 14.** The  $g - r$  colour, sSFR, active fraction, stellar metallicity, and star forming gas metallicity as a function of stellar mass for central galaxies in different environments. Red, cyan, blue, and green curves denote the median values in knots, filaments, sheets, and voids, respectively. Each dot represent an individual galaxy with the same colour coding as the curves. Errors are generated using the bootstrap method.

stellar masses below  $1.8 \times 10^{10} h^{-1} M_{\odot}$  and also decreases towards high masses. The absolute values are lower in knots both at low and high masses compared to other environments, but is higher at the turn over mass.

In summary, for the colour versus stellar mass relation and sSFR versus stellar mass relation, the combined dependence follows the pure cosmic web dependence at low masses quantitatively, while at high masses, the combined dependence is stronger. For the stellar metallicity versus stellar mass, the combined dependence mimic the pure cosmic web dependence at high masses, but vanishes at low masses. The gas metallicity versus stellar mass relation behaves significantly different in knots compared to other environments and the combined dependence deviate from the pure cosmic web dependence at all masses.

## 5 CONCLUSIONS

In this paper, we investigate the dependence of galaxy properties on different cosmic web environments and their evolution, using

the EAGLE cosmological hydrodynamical simulations. We split the simulation box into  $256^3$  cells and generate the web elements adopting the web classification method of Hahn et al. (2007). Here, we summarize our results as follows.

We find the baryon fraction increases with halo mass in all environments and the fraction is higher in denser regions, i.e. increasing along the sequence voids, sheets, filaments, and knots. This environmental dependence persists up to  $z = 6$ . The cosmic web dependence becomes slightly stronger at higher redshifts up to  $z \sim 3$  and then becomes weaker towards even higher redshifts. The central and total stellar mass-to-halo mass ratios both peak at halo masses  $\sim 10^{12} h^{-1} M_{\odot}$ . At low masses, more stars are formed in knots than in other web environments, while at high masses, less stars are formed in knots. The cosmic web dependence of the galaxy stellar mass functions is very strong at all redshifts, with the amplitude decreasing along the sequence knots, filaments, sheets, and voids. Interestingly, though the average characteristic stellar mass corresponding to  $L^*$  does not evolve much since  $z = 1$ , it changes by an order of magnitude going from knots to voids at  $z = 0$ .



We remove the halo mass dependence and investigate the relation between the cosmic web and various scaling relations for central galaxies. We find a characteristic stellar mass of  $1.8 \times 10^{10} h^{-1} M_{\odot}$ , below and above which the cosmic web dependence behaves oppositely. Galaxies with stellar mass below the characteristic mass are redder, with lower active fraction, lower sSFR, and higher stellar metallicity in knots than in voids, while at stellar masses above the characteristic mass, the dependences on the cosmic web either reverse or vanish. At low masses, the relatively strong web dependences of the colour versus stellar mass relation and of the sSFR versus stellar mass relation can be attributed to the cosmic web dependence of the active galaxy fraction, i.e. the active fraction is higher in voids than in knots. For active galaxies, the stellar metallicity is higher in knots compared to other web environments for those with stellar mass below the characteristic mass.

The cosmic web dependences are weaker at higher redshifts for almost all the galaxy properties and scaling relations we explored, including the central (total) stellar-to-halo mass ratio, colour versus stellar mass relation, sSFR versus stellar mass relation, and stellar metallicity versus stellar mass relation. But this is not the case for the gas metallicity versus stellar mass relation. For galaxies above the characteristic stellar mass, this cosmic web dependence gets even stronger at high redshifts, decreasing along the sequence voids, sheets, filaments, and knots.

The combined halo + cosmic web dependence follows the cosmic web dependence at low masses for the colour/sSFR versus stellar mass relations, but is stronger at high masses. It reverses for the stellar metallicity at high masses, the combined dependence mimics the cosmic web dependence, while at low masses, the combined dependence almost vanishes. One can not use the combined dependence of gas metallicity relation versus stellar mass relation to explore the pure cosmic web dependence at all for they behave different at all masses.

## ACKNOWLEDGEMENTS

We thank Yingjie Jing and Marius Cautun for helpful discussion. This work is supported by the National Key Research and Development of China (Nos 2018YFA0404503, 2016YFA0400703, and 2016YFA0400702) and the National Natural Science Foundation of China (NSFC; 11573033, 11622325, 11133003, 11425312, 11733010, 11633004). LG also acknowledges the National Key Program for Science and Technology Research Development (2017YFB0203300). CGL was supported by the Science and Technology Facilities Council [ST/P000541/1]. XC also acknowledges the NSFC-ISF joint research program no. 11761141012, the CAS Frontier Science Key Project QYZDJ-SSW-SLH017, Chinese Academy of Sciences (CAS) Strategic Priority Research Program XDA15020200, and the MOST 2016YFE0100300, 2018YFE0120800. QG, LG, and CGL acknowledge support from the Royal Society Newton Advanced Fellowships. This equipment was funded by BIS National E-infrastructure capital grant ST/K00042X/1, STFC capital grant ST/H008519/1, and STFC DiRAC Operations grant ST/K003267/1 and Durham University. DiRAC is part of the National E-Infrastructure.

## DATA AVAILABILITY

The data presented in this article are available at the EAGLE simulations public data base (<http://icc.dur.ac.uk/Eagle/database.php>).

## REFERENCES

- Alpaslan M. et al., 2015, *MNRAS*, 451, 3249  
 Baldry I. K., Balogh M. L., Bower R. G., Glazebrook K., Nichol R. C., Bamford S. P., Budavari T., 2006, *MNRAS*, 373, 469  
 Beare R., Brown M. J. I., Pimblet K., Taylor E. N., 2019, *ApJ*, 873, 78  
 Brouwer M. M. et al., 2016, *MNRAS*, 462, 4451  
 Cen R., Ostriker J. P., 1999, *ApJ*, 514, 1  
 Chen Y.-C. et al., 2017, *MNRAS*, 466, 1880  
 Codis S., Pichon C., Devriendt J., Slyz A., Pogosyan D., Dubois Y., Sousbie T., 2012, *MNRAS*, 427, 3320  
 Cucciati O., Iovino A., Kovač K., 2011, *Astrophys. Space Sci. Proc.*, 27, 171  
 Cui W. et al., 2019, *MNRAS*, 485, 2367  
 Dalla Vecchia C., Schaye J., 2012, *MNRAS*, 426, 140  
 Darvish B., Mobasher B., Sobral D., Rettura A., Scoville N., Faisst A., Capak P., 2016, *ApJ*, 825, 113  
 Darvish B., Mobasher B., Martin D. C., Sobral D., Scoville N., Stroe A., Hemmati S., Kartaltepe J., 2017, *ApJ*, 837, 16  
 Davé R. et al., 2001, *ApJ*, 552, 473  
 Davis M., Efstathiou G., Frenk C. S., White S. D. M., 1985, *ApJ*, 292, 371  
 De Rossi M. E., Theuns T., Font A. S., McCarthy I. G., 2015, *MNRAS*, 452, 486  
 De Rossi M. E., Bower R. G., Font A. S., Schaye J., Theuns T., 2017, *MNRAS*, 472, 3354  
 Dolag K., Borgani S., Murante G., Springel V., 2009, *MNRAS*, 399, 497  
 Dubois Y. et al., 2014, *MNRAS*, 444, 1453  
 Eardley E. et al., 2015, *MNRAS*, 448, 3665  
 Eckert D. et al., 2015, *Nature*, 528, 105  
 Ellison S. L., Patton D. R., Simard L., McConnachie A. W., 2008, *AJ*, 135, 1877  
 Forero-Romero J. E., Hoffman Y., Gottlöber S., Klypin A., Yepes G., 2009, *MNRAS*, 396, 1815  
 Ganeshiah Veena P., Cautun M., van de Weygaert R., Tempel E., Jones B. J. T., Rieder S., Frenk C. S., 2018, *MNRAS*, 481, 414  
 Gay C., Pichon C., Le Borgne D., Teyssier R., Sousbie T., Devriendt J., 2010, *MNRAS*, 404, 1801  
 Goh T. et al., 2019, *MNRAS*, 483, 2101  
 Guo Q. et al., 2011, *MNRAS*, 413, 101  
 Hahn O., Porciani C., Carollo C. M., Dekel A., 2007, *MNRAS*, 375, 489  
 Haider M., Steinhauser D., Vogelsberger M., Genel S., Springel V., Torrey P., Hernquist L., 2016, *MNRAS*, 457, 3024  
 Khandai N., Di Matteo T., Croft R., Wilkins S., Feng Y., Tucker E., DeGraf C., Liu M.-S., 2015, *MNRAS*, 450, 1349  
 Kraljic K. et al., 2018, *MNRAS*, 474, 547  
 Liao S., Gao L., 2019, *MNRAS*, 485, 464  
 Libeskind N. I. et al., 2018, *MNRAS*, 473, 1195  
 Mannucci F., Cresci G., Maiolino R., Marconi A., Gnerucci A., 2010, *MNRAS*, 408, 2115  
 Martizzi D., Vogelsberger M., Torrey P., Pillepich A., Hansen S. H., Marinacci F., Hernquist L., 2020, *MNRAS*, 491, 5747  
 Matthee J., Schaye J., 2019, *MNRAS*, 484, 915  
 Metuki O., Libeskind N. I., Hoffman Y., Crain R. A., Theuns T., 2015, *MNRAS*, 446, 1458  
 Moster B. P., Naab T., White S. D. M., 2013, *MNRAS*, 428, 3121  
 Peirani S., Jung I., Silk J., Pichon C., 2012, *MNRAS*, 427, 2625  
 Peng Y.-j. et al., 2010, *ApJ*, 721, 193  
 Planck Collaboration et al., 2014, *A&A*, 571, A1  
 Poudel A., Heinämäki P., Tempel E., Einasto M., Lietzen H., Nurmi P., 2017, *A&A*, 597, A86  
 Rosas-Guevara Y. M. et al., 2015, *MNRAS*, 454, 1038  
 Schaye J. et al., 2015, *MNRAS*, 446, 521  
 Schaye J., Dalla Vecchia C., 2008, *MNRAS*, 383, 1210  
 Scoville N. et al., 2013, *ApJS*, 206, 3  
 Sefusatti E., Crocce M., Scoccimarro R., Couchman H. M. P., 2016, *MNRAS*, 460, 3624  
 Sobral D., Best P. N., Smail I., Geach J. E., Cirasuolo M., Garn T., Dalton G. B., 2011, *MNRAS*, 411, 675  
 Springel V., 2005, *MNRAS*, 364, 1105



- Springel V., White S. D. M., Tormen G., Kauffmann G., 2001, *MNRAS*, 328, 726
- Springel V., Di Matteo T., Hernquist L., 2005, *MNRAS*, 361, 776
- Tempel E., Kipper R., Saar E., Bussov M., Hektor A., Pelt J., 2014, *A&A*, 572, A8
- Trayford J. W. et al., 2015, *MNRAS*, 452, 2879
- Vogelsberger M. et al., 2014, *MNRAS*, 444, 1518
- Wiersma R. P. C., Schaye J., Smith B. D., 2009a, *MNRAS*, 393, 99
- Wiersma R. P. C., Schaye J., Theuns T., Dalla Vecchia C., Tornatore L., 2009b, *MNRAS*, 399, 574
- Yan H., Fan Z., White S. D. M., 2013, *MNRAS*, 430, 3432
- Yates R. M., Kauffmann G., Guo Q., 2012, *MNRAS*, 422, 215
- Zhang Y., Yang X., Faltenbacher A., Springel V., Lin W., Wang H., 2009, *ApJ*, 706, 747
- Zhu W., Feng L.-L., 2017, *ApJ*, 838, 21

This paper has been typeset from a  $\text{\LaTeX}$  file prepared by the author.